Interrogating the composition and genesis of argillite-hosted pyrite nodules at the LaRonde Penna gold-rich volcanogenic massive sulphide deposit, Abitibi, Quebec: Insights into metallogenic implications

Jean-Luc Pilote[1*], Patrick Mercier-Langevin[1], Simon E. Jackson[2], Benoît Dubé[1], Zhaoping Yang[2], Christopher J.M. Lawley[2], Duane C. Petts[2], Graham D. Layne[3], and Stephen J. Piercey[3]

[1]Geological Survey of Canada, 490 rue de la Couronne, Québec, Quebec G1K 9A9
[2]Geological Survey of Canada, 601 Booth Street, Ottawa, Ontario K1A 0E8
[3]Memorial University of Newfoundland, St. John's, Newfoundland A1B 3X5
[*]Corresponding author's e-mail: jean-luc.pilote@canada.ca

ABSTRACT

This study investigates pyrite nodules hosted in argillite horizons within (Zn-Ag-Au-Cu±Pb) massive sulphide ore of the 20N Zn zone at the LaRonde Penna Au-rich volcanogenic massive sulphide deposit, Abitibi greenstone belt, Quebec. Two pyrite nodules are examined in detail: LA-001 and LA-002. These nodules are spherical and oblate spheroidal in shape and display similar textures, including a core (zone 1) composed of fine, equigranular grains with variable amounts of silicate-carbonate inclusions; a rim (zones 2a to c) that varies from inclusion-poor to -rich and consists of equigranular to radially oriented, acicular pyrite grains; and a thin layer of idiomorphic pyrite overgrowth that surrounds the nodules (zone 3). Sulphide inclusions in nodule LA-001 consist predominantly of sphalerite, whereas sulphide inclusions in nodule LA-002 include an assemblage of sphalerite, Zn-bearing stannite ($Cu_2(Fe,Zn)SnS_4$), and galena, all of which occur also in the surrounding massive sulphide ore. In nodule LA-002, sphalerite is intimately associated with stannite, and together they are preferentially concentrated along both the concentric zones of the inclusion-rich section of the rim (zone 2b) and within the radially bladed rim (zone 2c), parallel to blade elongation. Whereas textures are similar in the two nodules, compositional maps generated by laser ablation-inductively coupled plasma-mass spectrometry (LA-ICP-MS) reveal important distinctions in element distribution patterns for inclusion-partitioned elements (Cu, Zn, Sn, Pb, Bi), which reflect the mineralogy and bulk abundances for lattice-bound elements (Ni, As, Au). Gold is mainly concentrated in the fine-grained cores, but in different amounts in LA-001 (average of 0.38 ppm Au; n = 6918) and LA-002 (average of 1.04 ppm Au; n = 10,539). Nickel and As values in LA-001 are respectively 10 and 3 times greater than in LA-002. In both nodules, Ni is enriched in the rim relative to the core. The pyrite nodules have in situ $\delta^{34}S$ values (secondary ion mass spectrometry analyses) that range from -0.8 to +5.0‰ (average +2.1‰, n = 50), with the core showing slightly lighter values than the rim. Based on these results, the nodules (zones 1 and 2) are interpreted to have formed by diagenetic processes and the presence of stannite, sphalerite, and galena (enrichment in Zn, Sn, Cu, and Pb) is likely the expression of a previously hydrothermally enriched sediment rather than a direct hydrothermal contribution during crystal growth. While more work is needed, the composition of pyrite nodules could potentially be used as vectors toward syngenetic mineralization.

INTRODUCTION

The LaRonde Penna deposit is an Au-rich volcanogenic massive sulphide (VMS; ~9 Moz Au) hosted in the upper part of the 2704–2695 Ma Blake River Group (Fig. 1) in the southern Abitibi greenstone belt (Mercier-Langevin et al., 2017). Thin argillite layers occur within the main sulphide orebody of the 20 North lens in the uppermost levels of the mine (≤1700 m below surface: Dubé et al., 2004; Mercier-Langevin et al., 2007b) and host centimetre-scale pyrite nodules that share textural similarities with diagenetic pyrite nodules reported in various ancient and modern sedimentary sequences around the world (e.g. Guy et al., 2010, 2014; Rickard, 2012; Gregory et al., 2019). In some areas (e.g. Timmins district) pyrite nodules can host significant amounts of Au (up to >10 ppm Au; Pilote et al., 2019, 2020). Over the past few decades, the origin of Au at LaRonde and other VMS deposits in the Doyon-Bousquet-LaRonde mining camp has been a source of much controversy. Various models have been

Pilote, J.-L., Mercier-Langevin, P., Jackson, S.E., Dubé, B., Yang, Z., Lawley, C.J.M., Petts, D.C., Layne, G.D., and Piercey, S.J., 2020. Interrogating the composition and genesis of argillite-hosted pyrite nodules at the LaRonde Penna gold-rich volcanogenic massive sulphide deposit, Abitibi, Quebec: Insights into metallogenic implications; *in* Targeted Geoscience Initiative 5: Contributions to the Understanding of Canadian Gold Systems, (ed.) P. Mercier-Langevin, C.J.M. Lawley, and S. Castonguay; Geological Survey of Canada, Open File 8712, p. 75–91. https://doi.org/10.4095/323666

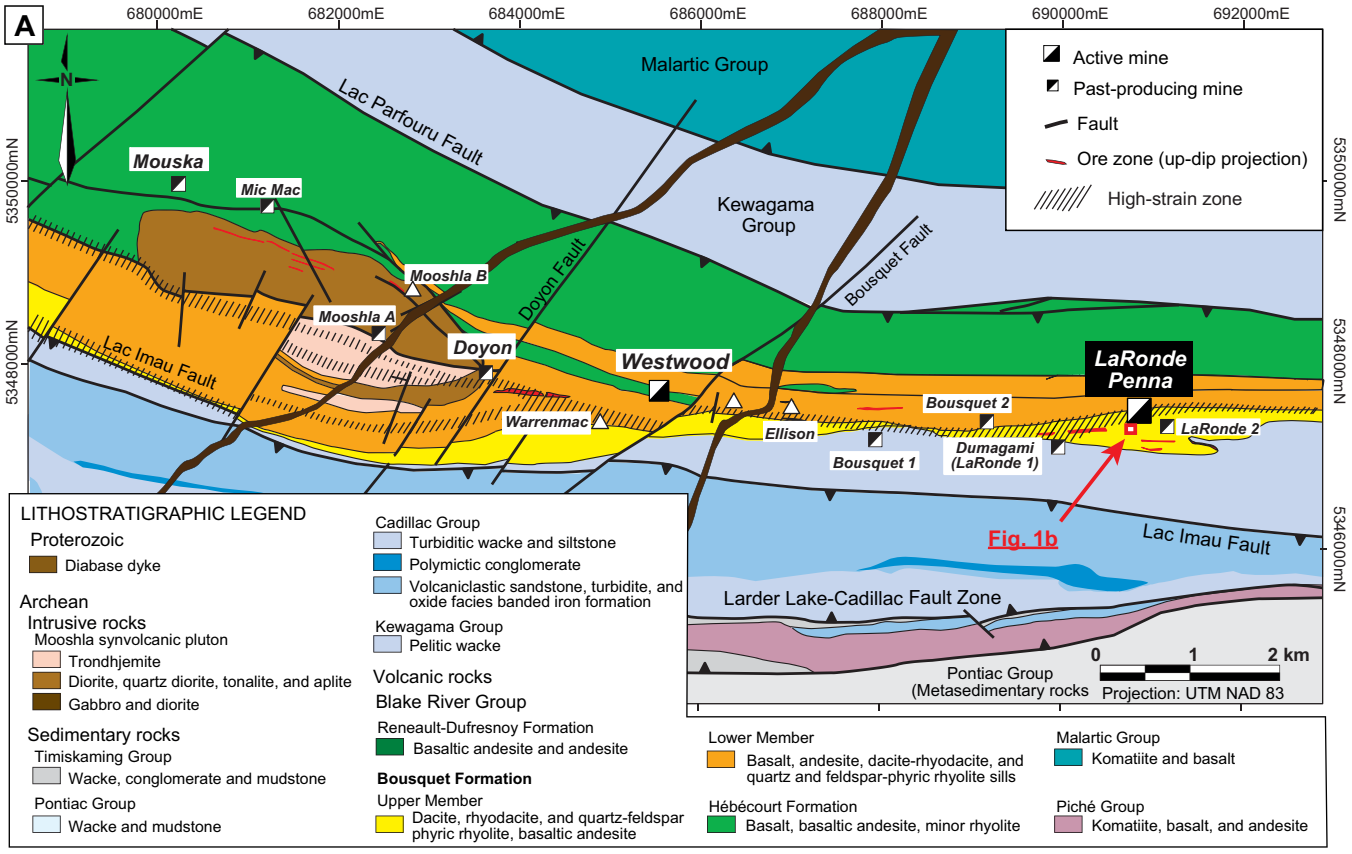

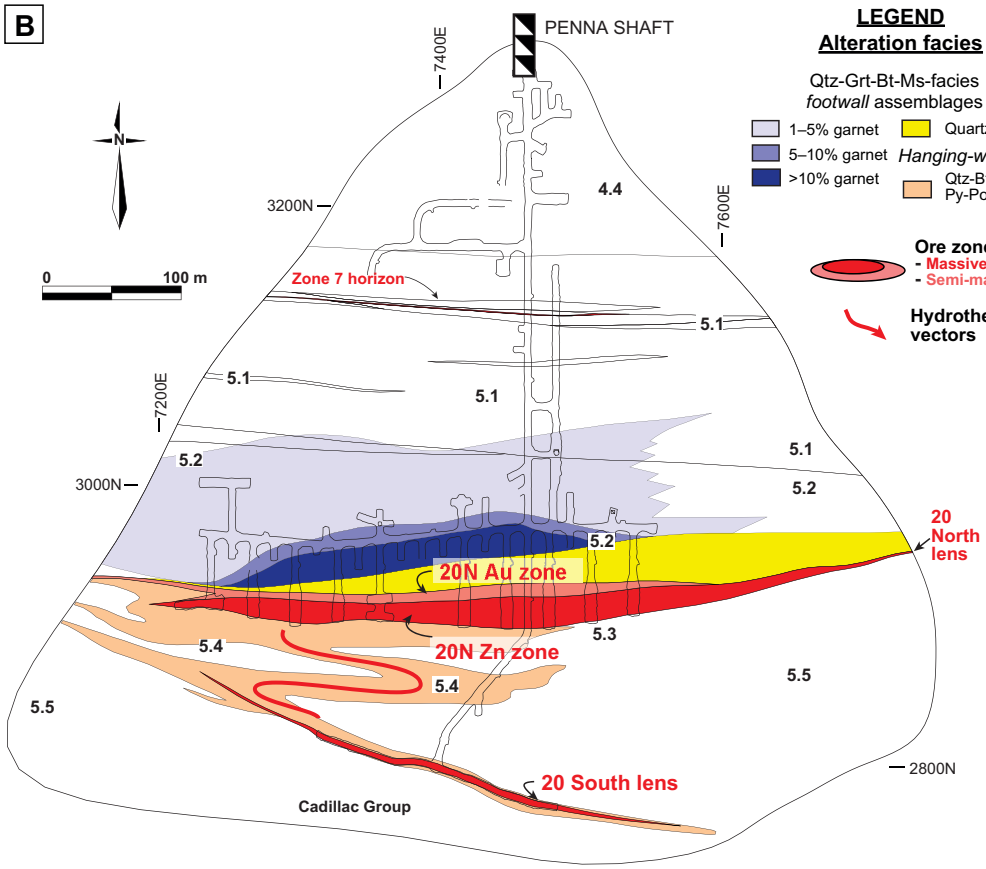

Figure 1. a) Simplified geology of the Doyon-Bousquet-LaRonde mining camp showing the location of the LaRonde Penna deposit. *Modified after* Mercier-Langevin et al. (2017). **b)** Map of level 146 (1460 m depth) of the LaRonde Penna mine showing the distribution of the upper units of the Bousquet Formation, ore zone 7, the 20 North and 20 South lenses, and the distribution of the main alteration assemblages. *Modified after* Mercier-Langevin et al. (2017). Abbreviations: Ab = albite; Bt = biotite, Grt = garnet, Ms = muscovite, Po = pyrrhotite, Py = pyrite, Qtz = quartz, Rt = rutile, Ttn= titanite.

proposed, including the following: 1) synvolcanic or syngenetic Au enrichment; 2) multi-stage Au enrichment with the Au being structurally introduced and/or remobilized into high-strain zones; and 3) epigenetic (syndeformation) Au enrichment (Mercier-Langevin et al., 2017, and references therein). An improved understanding of processes responsible for the genesis of deposits in modern systems, fossil hydrothermal systems and reconstruction of the Doyon-Bousquet-LaRonde mining camp geology have provided substantial insights into the synvolcanic and/or syngenetic model for the introduction of Au in the VMS deposits of the camp, including LaRonde (to cite only a few, Sillitoe et al., 1996; Hannington et al., 1999b, 2005; Dubé et al., 2007a,b, 2014; Mercier-Langevin et al., 2007b,c; Monecke et al., 2008, 2009). Given that nodules can incorporate significant amounts of Au, constraining the timing and factors controlling this enrichment could provide another line of evidence for the timing of Au introduction in VMS deposits, which can be helpful in understanding complex and/or understudied metamorphosed syngenetic systems elsewhere. Also, because nodules can host a number of trace elements (e.g. Zn, Cd, and Cu as inclusions; Co, Ni, Se, and Te as stoichiometric substitutions; and As, Tl, Au, Mo, Pb, Ag, Sb, Bi, and Mn as non-stoichiometric substitutions; Large et al., 2007, 2014) and can co-exist with the mineralization at LaRonde, understanding their compositions can provide further, independent constraints into the local paleoconditions (e.g. redox) of this world-class Au-rich VMS system.

Previous work concluded that part of the mineralization at LaRonde formed by sub-seafloor replacement rather than seafloor accumulation (Dubé et al., 2007b; Mercier-Langevin et al., 2007b) and, moreover, that the deposition of argillite was likely contemporaneous with the hydrothermal activity that formed the sulphide lens (Dubé et al., 2004, 2007b). Because of the seafloor and sub-seafloor replacement-style sulphide deposition, the formation of nodules in argillite lenses in the massive sulphide zones could have been contemporaneous with the hydrothermal activity. The ore lenses at the LaRonde Penna deposit vary in mineralogy, style, and metal composition, which relates to the protracted nature of the system and the compositionally evolving ore-forming fluids (Dubé et al., 2004, 2007a,b). Therefore, the nodules are a potential record of direct or indirect evidence of hydrothermal activity, and variations in mineralogical and chemical compositions may possibly record the evolving, Au-rich hydrothermal system. The objectives of this contribution, which forms part of a broader study on Archean sulphide nodules (*see* Pilote et al., 2020), involve characterization of the mineralogy, textures, and chemical and S-isotope compositions of the LaRonde Penna pyrite nodules, and discussion of their possible metallogenic and exploration implications.

GEOLOGICAL CONTEXT

Only a brief overview of the regional geological setting and deposit geology is presented here. Readers are encouraged to read Monecke et al. (2017), and references therein, for a geology review of the southern Abitibi greenstone belt and Dubé et al. (2007a,b) and Mercier-Langevin et al. (2007a,b,c) for details about the geology of the LaRonde Penna deposit.

The LaRonde Penna deposit is hosted by volcanic rocks of the eastern Blake River Group, which is structurally bounded to the north by the southeast-northwest-oriented Lac Parfouru fault zone (Fig. 1a). This fault separates the Blake River Group from the sedimentary rocks of the ≤2687 Ma (Davis, 2002) Kewagama Group. To the south, the Blake River Group is overlain by sedimentary rocks of the Cadillac Group (≤2689 Ma in the LaRonde deposit area: Mercier-Langevin et al., 2007b). Further to the south, the sedimentary rocks of the Cadillac Group are truncated by the east-west-striking Larder Lake-Cadillac fault zone.

The LaRonde deposit is hosted by the south-younging 2699–2697 Ma Bousquet Formation (Blake River Group: Lafrance et al., 2003; Mercier-Langevin et al., 2007b; McNicoll et al., 2014), which is divided into lower and upper members (Lafrance et al., 2003; Mercier-Langevin et al., 2007b). The 200 to 600 m thick lower member (unit 4.4 in Fig. 1b) is dominated by mafic to intermediate and tholeiitic to transitional rocks, whereas the upper member (units 5.1 to 5.5 in Fig. 1b) mostly comprises felsic volcanic and shallow intrusive rocks of transitional to calc-alkaline magmatic affinity (Lafrance et al., 2003; Mercier-Langevin et al., 2007b,c). The latter forms flows, lobes, flow-breccia deposits, and sill complexes of basalt and andesitic to rhyolitic compositions.

The ore lenses of the LaRonde deposit are hosted in the volcanic flows and volcaniclastic rocks of the upper member of the Bousquet Formation (Fig. 1b) and are characterized by semi-massive to massive sulphides or narrow intervals of transposed sulphide veins and veinlets. The lenses are spatially associated with several metamorphosed alteration assemblages developed in both the stratigraphic footwall and hanging-wall volcanic units (Dubé et al., 2007b). The stacked ore lenses represent different episodes of sulphide precipitation in a single protracted hydrothermal system (Dubé et al., 2007a; Mercier-Langevin et al., 2007b). In the upper stratigraphic part of the deposit, the 20 North lens comprises a transposed pyrite-chalcopyrite (Au-Cu) stockwork (20N Au zone), which is directly overlain by a pyrite-sphalerite-galena-chalcopyrite-pyrrhotite (Zn-Ag-Pb) massive sulphide lens (20N Zn zone).

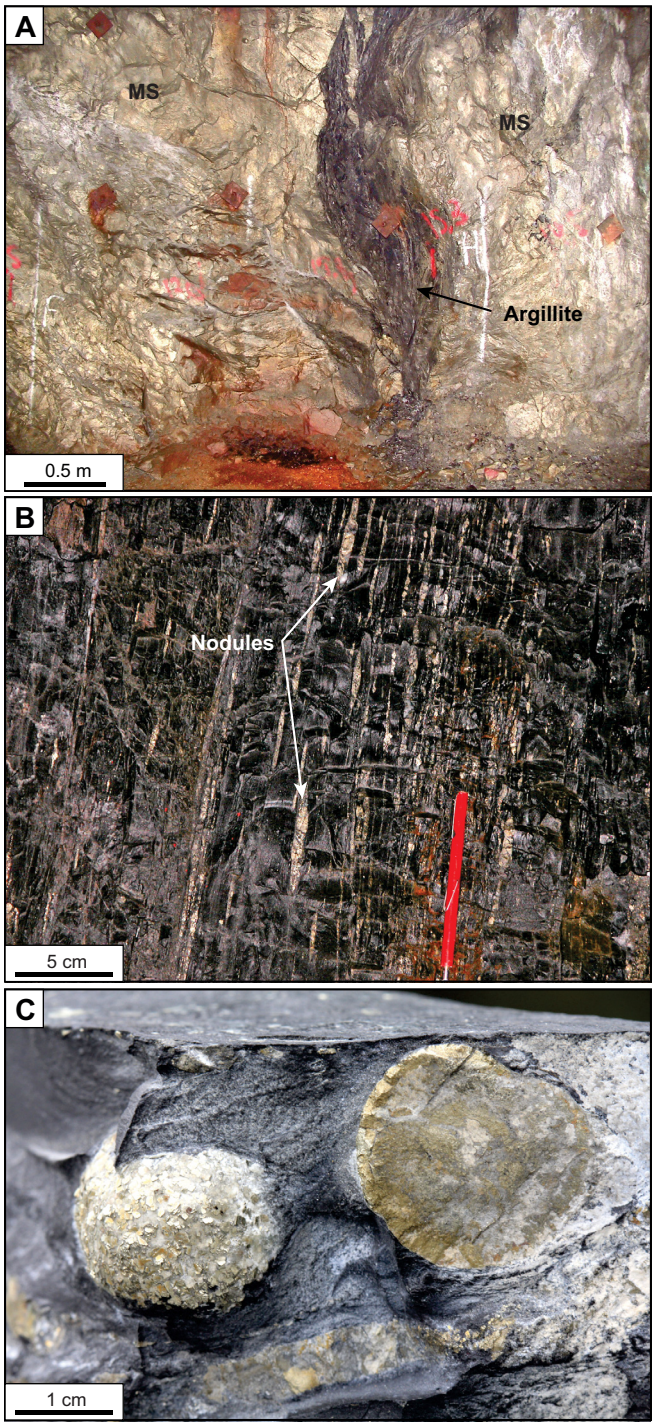

Figure 2. a) 20N Zn zone massive sulphide lens (pyrite, sphalerite±galena, chalcopyrite, pyrrhotite) enclosing a highly strained graphitic argillite lens (stope 152-20-66 west wall, 1520 m below surface). **b)** Strongly deformed (flattened ±stretched) pyrite nodules in siliceous graphitic argillite, stope 131-20-70 west wall, 1310 m below surface. **c)** Pyrite nodules in a graphitic argillite unit. The section view of the nodule to the right shows a perfectly preserved concentric zonation, whereas the nodule to the left is complete and shows a granoblastic outer rim (sample courtesy of D. Pitre). Abbreviation: MS = massive sulphide.

Discontinuous argillite layers are found within the massive sulphide lens of the 20N Zn zone that, because of their low competency relative to the sulphides, generally accommodate much of the tectonic strain (Fig. 2a: Mercier-Langevin et al., 2007b). Abundant centimetre-scale pyrite nodules are present in these sedimentary layers and are generally strongly deformed (Fig. 2b,c), although some remain locally unstrained. Late quartz-carbonate veins are also abundant in these argillitic units, crosscutting both the nodules and their enclosing sedimentary rock.

RESULTS

Nodule Mineralogy and Textures

Unstrained nodules from the argillite in the 20N Zn zone are round to slightly oblate and generally less than two centimetres in diameter (Fig. 2c, 3a,b). Pyrite forms most of the mass of the nodules, with inclusions that vary in abundance, distribution, and composition. The inclusions are composed of quartz, chlorite±mica, calcite, and other sulphide minerals. Two samples were studied in detail (LA-001 and LA-002) and both show concentric zones that are reflected by the distribution of inclusions or a change in the crystal habit of pyrite (Fig. 3a–c, 4a). Nodule LA-001 is spherical (Fig. 3a), whereas LA-002 is slightly elongated (Fig. 3b), forming an oblate spheroid with its flattening parallel to the main foliation in the argillite.

Based on their textures, three main growth zones can be distinguished (Fig. 4a). The innermost zone (or "core") is composed of very fine, polycrystalline pyrite with abundant calcite-silicate material (zone 1; Fig. 3a,b, 4a,b). While polishing the samples for SIMS analysis, a thin massive pyrite corona was revealed, which surrounds the inclusion-rich core in LA-001 (subdivided into zones 1b and a, respectively). Zone 2 forms most of the outer mass of the nodules (or "rim") and is subdivided into three parts (zones 2a–c; Fig. 4a,b), which consist of an equigranular assemblage of very fine decussate- or sheaf-like grains (zone 2a), inclusion-rich concentric features (zone 2b), and a radially oriented acicular outer region (zone 2c). An overgrowth of euhedral, inclusion-poor pyrite, such as the one shown in Figure 2c, forms the outer edge of nodule LA-002 (zone 3; Fig. 3d, 4f). A similar overgrowth is developed on nodule LA-001 but separated during mounting of the sample in epoxy. This overgrowth is likely metamorphogenic and parts of it are possibly synchronous with the development of a quartz vein that truncates the nodule (Fig. 3e,f).

Sphalerite constitutes the dominant sulphide inclusion phase in nodule LA-001 where it is largely concentrated around the core (Fig. 3c). Pyrite nodule LA-002 contains inclusions with an assemblage of galena<

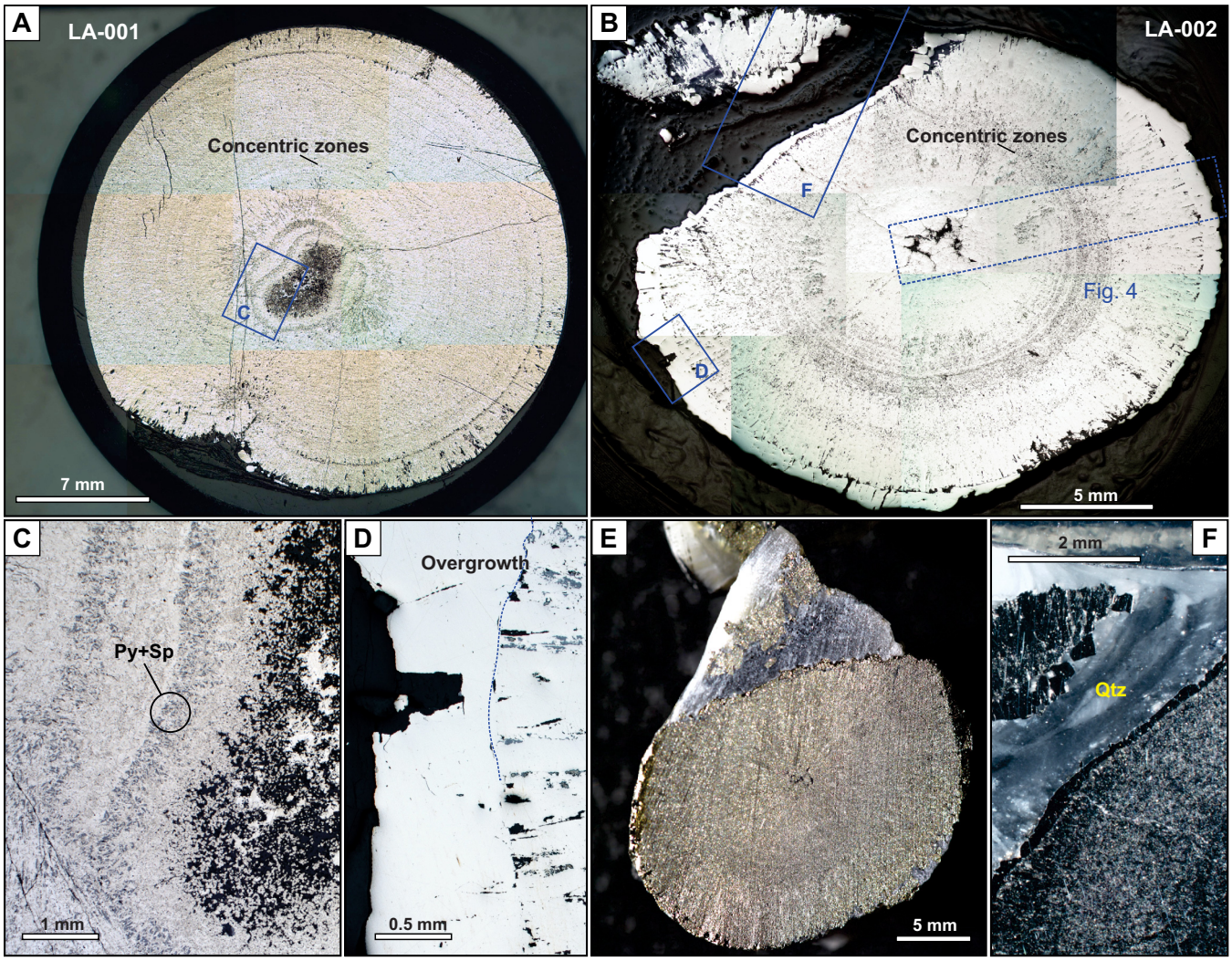

Figure 3. Representative photographs and photomicrographs of nodules LA-001 and LA-002 from the 20N Zn zone of the LaRonde Penna Au-rich VMS deposit. **a)** Nodule LA-001 in reflected light. **b)** Nodule LA-002 in reflected light. **c)** Close-up of (a) showing in the inclusion-rich core and concentric zones defined by abundant sphalerite (Sp) inclusions in the pyrite (Py) nodules. **d)** Close-up of (b) showing the idiomorphic nature of the overgrowth pyrite surrounding the nodule. **e)** Photograph of nodule LA-002 (unpolished) showing the crosscutting quartz veins. **f)** Close-up of (b) in natural light showing the dark grey quartz (Qtz) vein and the development of the inclusion-free pyrite overgrowth.

sphalerite≤stannite ($Cu_2(Fe,Zn)SnS_4$) (Fig. 4d,g–j) with most sulphide inclusions restricted to zones 1 and 2 as <40 µm sized grains (Fig. 4c-j); however, <500 µm sized galena grains are also found within overgrowth pyrite grain boundaries (Fig. 4f,j). The composition of stannite (semi-quantitative) was obtained by scanning electron microscope (SEM)-electron dispersive X-ray spectroscopy (EDS) and revealed Zn abundances averaging ~3 wt% Zn (Table 1). Sphalerite is typically in contact with stannite and together they concentrate along the main elongation of the nodules (and the acicular pyrite) and within the concentric, inclusion-rich zone (Fig. 4d–f,h–j). Galena is not spatially associated with the other two sulphides; however, galena is present outside the core and tends to be concentrated preferentially near the margin of the flattened nodule.

Geochemistry of Nodules

Methodology

Two-dimensional element content maps of the two nodules were generated by LA-ICP-MS (GSC-Ottawa) to allow quantitative determination of the distributions of Au and other major and trace elements (Fig. 5, 6). The areas mapped were sampled via tens of thousands of discrete edge-to-edge square ablation spots (with 3–5 "pre-ablation" laser pulses for surface cleaning, 1.5 s flush, and 2 s ablation). Quantification of the data from the multi-phase mineral assemblages was achieved via external calibration against United States Geological Survey synthetic basaltic glass reference material GSE-1G, coupled with ablation yield correction via normalization to 100% total element abundance (Halicz and Günther, 2004), performed on a spot-by-

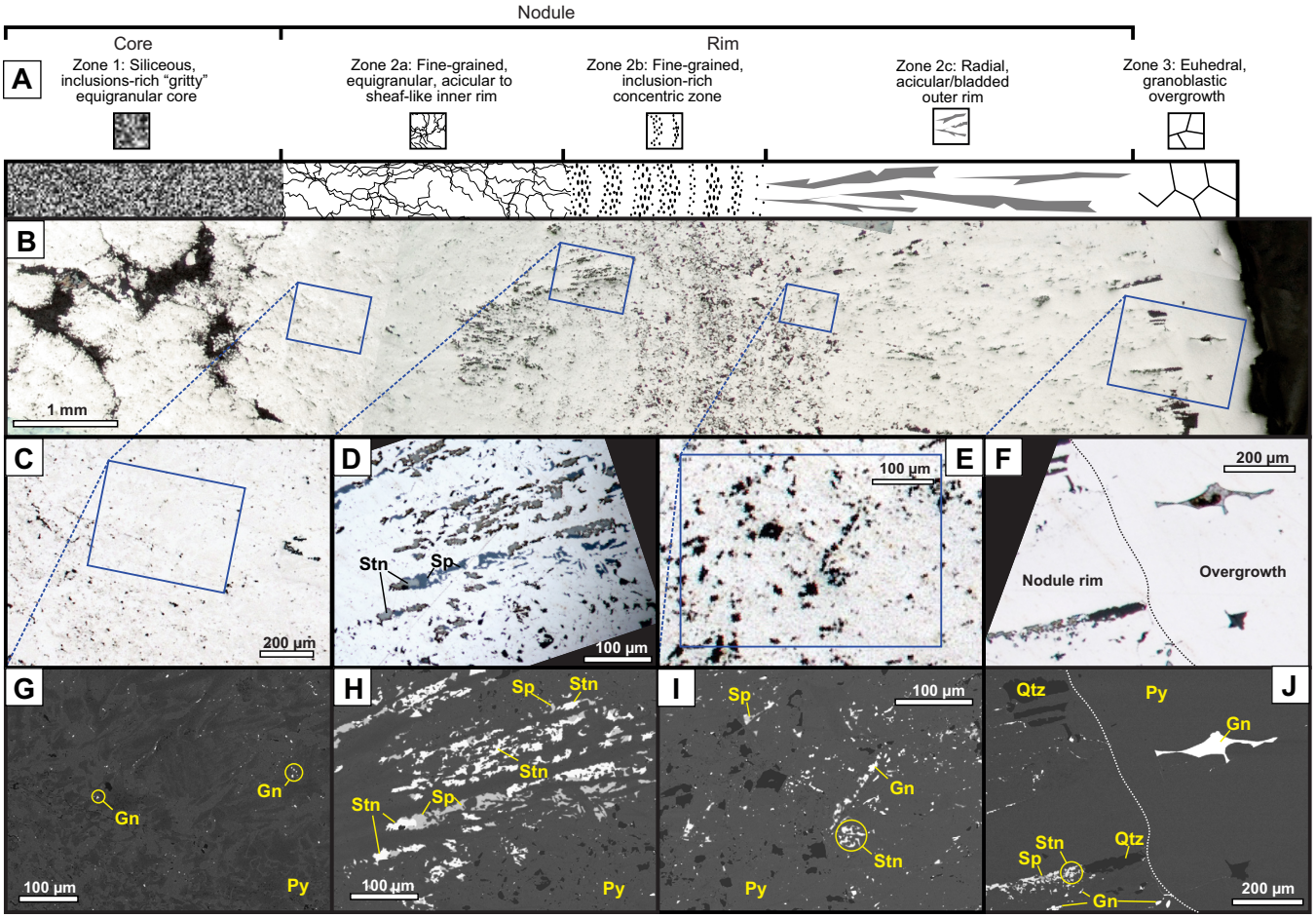

Figure 4. a) Schematic diagram showing the various zones composing pyrite nodule LA-002 based on textures. Note that zone 1b is absent in LA-002. **b)** Section close-up of Figure 3b. **c to f)** Episcopic images with respective regions shown in (b). **g to j)** Backscattered electron images (BSE) of (c) to (f). Abbreviations: Gn = galena, Py = pyrite, Qtz = quartz, Sp = sphalerite, Stn = stannite.

spot basis. To extend the calibration to S and C, which are not measurable in GSE-1G, surrogate calibration was applied using S/Fe and C/Ca sensitivity ratios determined by ablation of pure pyrrhotite and calcite, respectively. Data reduction was achieved using fully automated in-house spreadsheet software, LAMTrace, and its sister program, Convert (Jackson, 2008). Element contents for GSE-1G were GeoRem "preferred values" (http://georem.mpch-mainz.gwdg.de/). Another in-house spreadsheet program (PixeLAte) was used to generate element concentration maps by assembling and displaying element concentrations for each spot as coloured pixels using percentile or logarithmic scaling functions.

Trace element distribution

Element maps (Fig. 5, 6) show the general concentric zonation of the nodules, which are in agreement with petrographic observations. The presence of silicate inclusions in the cores and inside the rims is reflected by the abundance in Al_2O_3 (Fig. 5b, 6b). In nodule LA-001, Mn, Cu, Zn, Ag, Sn, Sb, Au, and Tl are most abun-

Table 1. Scanning electron microscopy analyses of stannite from LaRonde Penna Mine pyrite nodule LA-002.

Weight %						
S	31.34	31.85	32.64	31.16	30.66	31.38
Fe	11.17	10.72	11.60	10.34	10.61	10.82
Cu	27.37	26.21	26.12	26.84	27.07	25.84
Zn	2.28	2.67	2.43	3.19	3.60	3.54
Sn	27.85	28.55	27.21	28.48	28.06	28.41
Atomic %						
S	52.05	52.85	53.49	52.02	51.31	52.26
Fe	10.65	10.22	10.91	9.91	10.19	10.35
Cu	22.94	21.95	21.60	22.61	22.86	21.72
Zn	1.86	2.18	1.96	2.62	2.95	2.89
Sn	12.50	12.80	12.04	12.85	12.68	12.78

Analyses carried out at the Institut national de la recherche scientifique, Centre Eau Terre et Environnement in Québec City with an automated x-spectrometer Carl Zeiss EVO 50 Smart electron microprobe by energy dispersive X-ray spectrometry microanalysis system (EDS). Raw X-ray data were converted to elemental wt% by the Cameca PAP matrix correction program. Analyses done using a 20 kV accelerating voltage, 2 nA beam current, 5 µm electron beam with a counting time of 20 s.

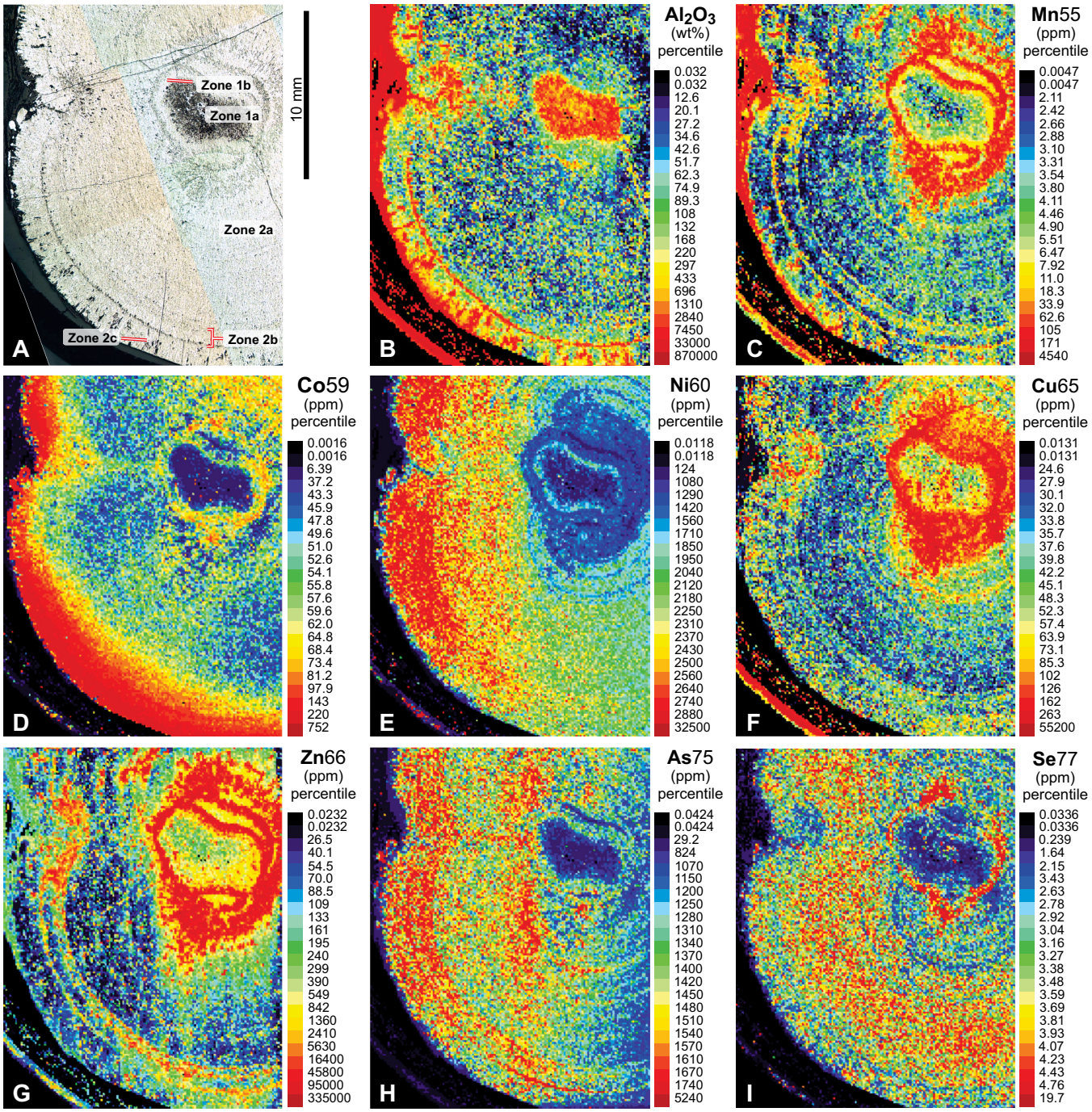

Figure 5. LA-ICP-MS element maps of pyrite nodule LA-001 from the 20N Zn zone of the LaRonde Penna Au-rich VMS deposit: **a)** episcopic image, **b)** Al_2O_3, **c)** Mn, **d)** Co, **e)** Ni, **f)** Cu, **g)** Zn, **h)** As, **i)** Se. All scales are in ppm, with the exception of Al_2O_3, which is in wt%. Figure is continued on the next page.

dant near or within the core, whereas As, Se, Te, Pb, and Bi are distributed more evenly across the nodule. Nickel and Co, however, are significantly enriched within and toward the outer rim (zones 2b and c).

In nodule LA-002, most elements decrease toward the rim except for Ni, Se, Pb, and Bi (Fig. 6); however, Mn, Co, Cu, Zn, Sn, Pb, and Bi also show localized concentrations that are either discordant to the concentric zones or follow them. High contents of Cu, Zn, and Sn correlate with the occurrence of sphalerite and stannite inclusions. High Pb and Bi contents correlate with galena inclusions. Although Au is concentrated in the core in both nodules, its highest content in nodule LA-001 overlaps areas that contain abundant sphalerite inclusions, whereas, in nodule LA-002, Au is evenly distributed within zones 1 and 2a.

The overgrowth envelope (zone 3) in nodule LA-002 is host to Co and Ni but contains lesser amounts of

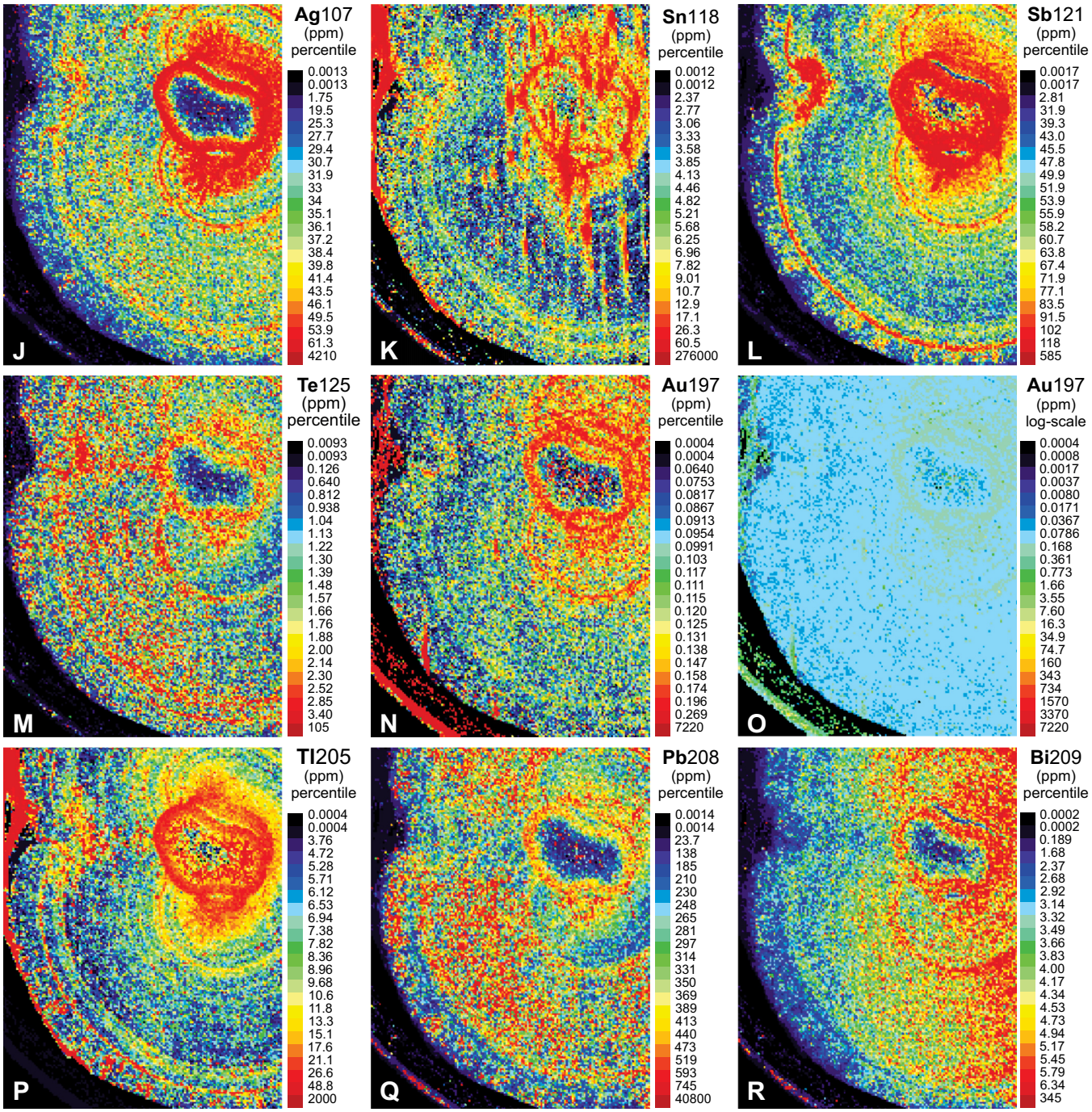

Figure 5 continued. LA-ICP-MS element maps of pyrite nodule LA-001 from the 20N Zn zone of the LaRonde Penna Au-rich VMS deposit: **j)** Ag, **k)** Sn, **l)** Sb, **m)** Te, **n)** Au (percentile scaling), **o)** Au (log scaling), **p)** Tl, **q)** Pb, **r)** Bi. All scales are in ppm.

other trace elements (Fig. 6d,e). Interestingly, whereas Co is enriched in most of the overgrowth pyrite grains, it is depleted in those formed along the quartz vein (Fig. 6d). Spotty, high concentrations of Pb and Bi in zone 3 can be explained by the presence of galena inclusions between overgrowth grain boundaries (Fig. 4f,j).

Comparison of Trace Element Abundance

Element concentrations derived from the LA-ICP-MS mapping are represented as violin plots in Figure 7. The two nodules show similar Mn, Co, Se, Ag, Sb, Te, and Tl values, whereas differences in mean values and/or highly variable concentrations of Ni, Cu, Zn, As, Sn, Au, Pb, and Bi were observed between nodules LA-001 and LA-002. For example, nodule LA-001 yielded Ni, Zn, As, and Bi concentrations that range from ~2 to 10 times greater than nodule LA-002. Apart from Zn (which preferably partitions into other sulphide phases over pyrite), the differences in Ni and As contents between the two nodules are noticeable (Fig.

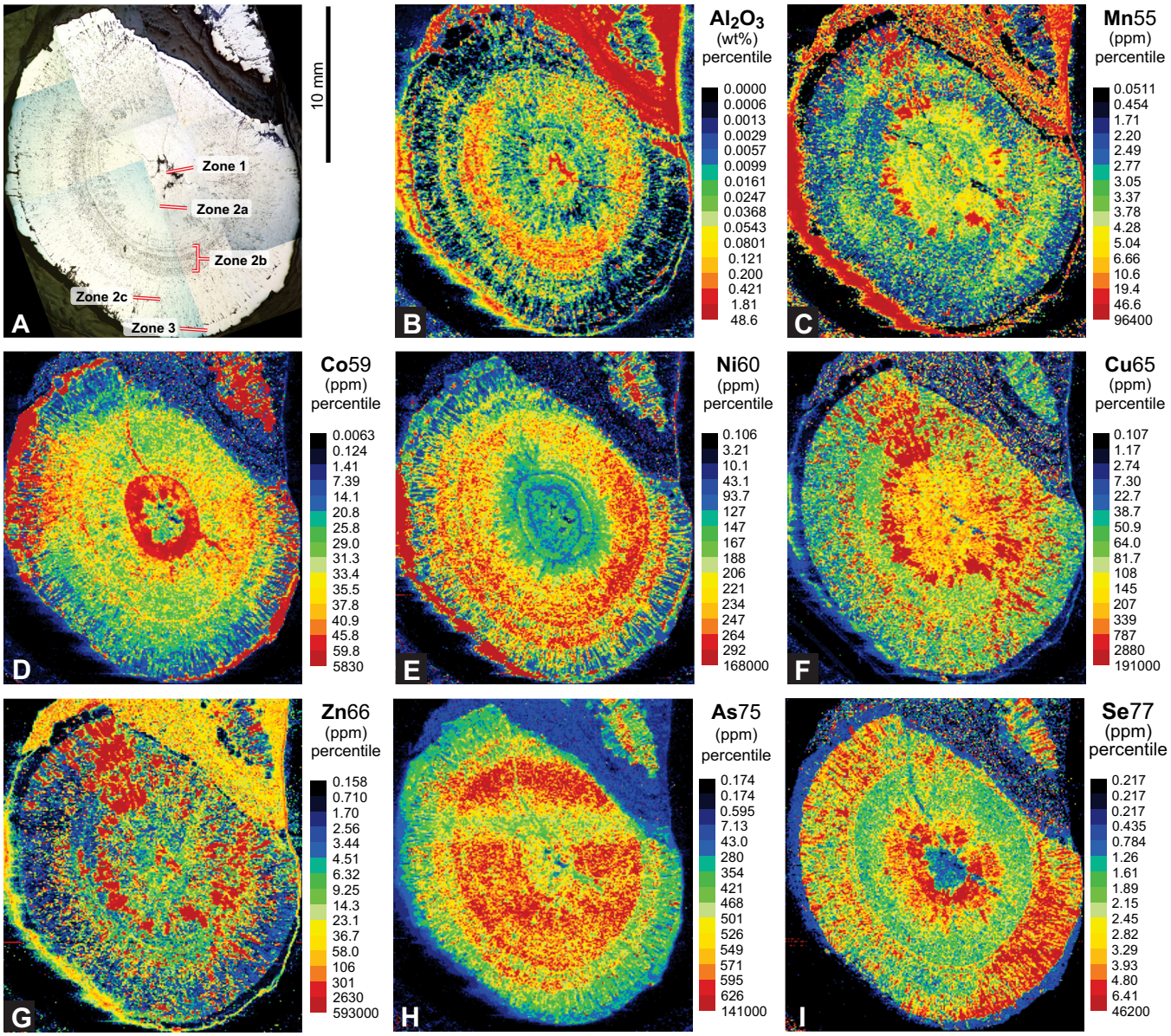

Figure 6. LA-ICP-MS element maps of pyrite nodule LA-002 from the 20N Zn zone of the LaRonde Penna Au-rich VMS deposit. **a)** episcopic image, **b)** Al_2O_3, **c)** Mn, **d)** Co, **e)** Ni, **f)** Cu, **g)** Zn, **h)** As, **i)** Se. All scales are in ppm, with the exception of Al_2O_3, which is in wt%. Figure is continued on the next page.

7c,f). Although Au is more abundant in nodule LA-002 by a factor of 2 to 3, both nodules have the highest Au concentrations in or near the core (Fig. 5n,o, 6n,o). Cores from nodules LA-001 and LA-002 average 0.38 ppm Au (n = 6918 pixels) and 1.04 ppm Au (n = 10,539 pixels), respectively. It is noteworthy that, although nodule LA-002 has more Au, it contains significantly less As than LA-001. This raises questions regarding the control of As on Au during trace element uptake and/or factors controlling the auriferous nature of the nodules (cf. Reich et al., 2005; Gregory et al., 2015), which is beyond the scope of this report but is an area currently being investigated by a broader study (Pilote et al., 2020).

Statistical analysis

Principal component analysis (PCA) is used to summarize the structure of the multivariate data set generated in this study (15 variables and 43,156 objects). Using the sulphide data from the LA-ICP-MS maps, principal components (PC) were computed in R software (R Core Team, 2019) after a log-transformation procedure to minimize any possible effects from closure and outliers (e.g. Filzmoser et al., 2009). For nodule LA-001 (Fig. 8a), most variance in the data is explained by the first PC (70.5%), which defines a strong separation between Zn and the rest of the trace elements. This can be explained by the presence of sphalerite inclusions, predominantly regulating Zn deportment. Similarly, the first PC also explains most of the variance (67.7%) in

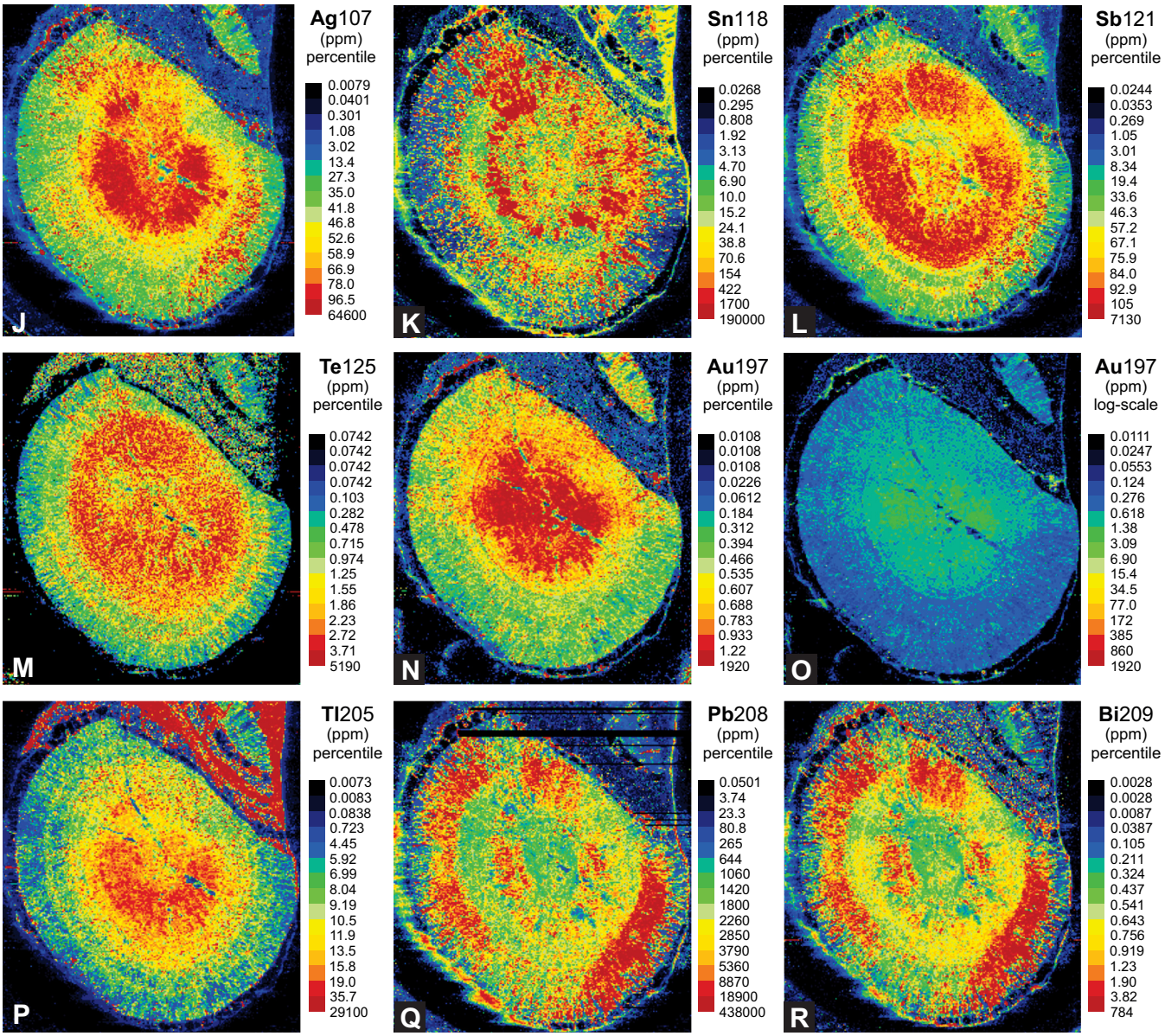

Figure 6 continued. LA-ICP-MS element maps of pyrite nodule LA-002 from the 20N Zn zone of the LaRonde Penna Au-rich VMS deposit: **j)** Ag, **k)** Sn, **l)** Sb, **m)** Te, **n)** Au (percentile scaling), **o)** Au (log scaling), **p)** Tl, **q)** Pb, **r)** Bi. All scales are in ppm.

nodule LA-002, with a strong separation of Zn, Sn, and Cu from the rest of the trace elements. The correlation between those three elements reflects the presence of sphalerite and Zn-bearing stannite ($Cu_2(Fe,Zn)SnS_4$) inclusions. Moreover, the strong correlation between Pb and Bi and their separation from the rest of the data in the second PC space (which explains 16.3% of the variance) concurs with the presence of galena in the nodule. The antithetic chemical relationship that exists between Zn-Cu-Sn and Bi-Pb from the PCA agrees with the lack of spatial association between sphalerite-stannite and galena, both from petrographic observations and from the distribution of the elements from the compositional maps. Elements that best mirror the overall Au distribution in nodule LA-001 (despite the low PC2 variance) are Co, Ni, Cu, As, Se, Sb, and Bi, and in LA-002, Te and Tl.

SULPHUR ISOTOPES

Methodology

Fifty sulphur isotope analyses were made on the nodules. Analyses were performed using the Cameca IMS 4f Secondary Ion Mass Spectrometer (SIMS) at the MAF-IIC Microanalysis Facility of Memorial University of Newfoundland. Samples were bombarded with a primary ion microbeam of 650–800 pA of Cs^+ accelerated through a nominal 10 keV potential, and focused into an 8–15 µm diameter spot following pre-sputtering for 120 s with a 25 μm^2 raster. Negatively charged sputtered secondary ions were

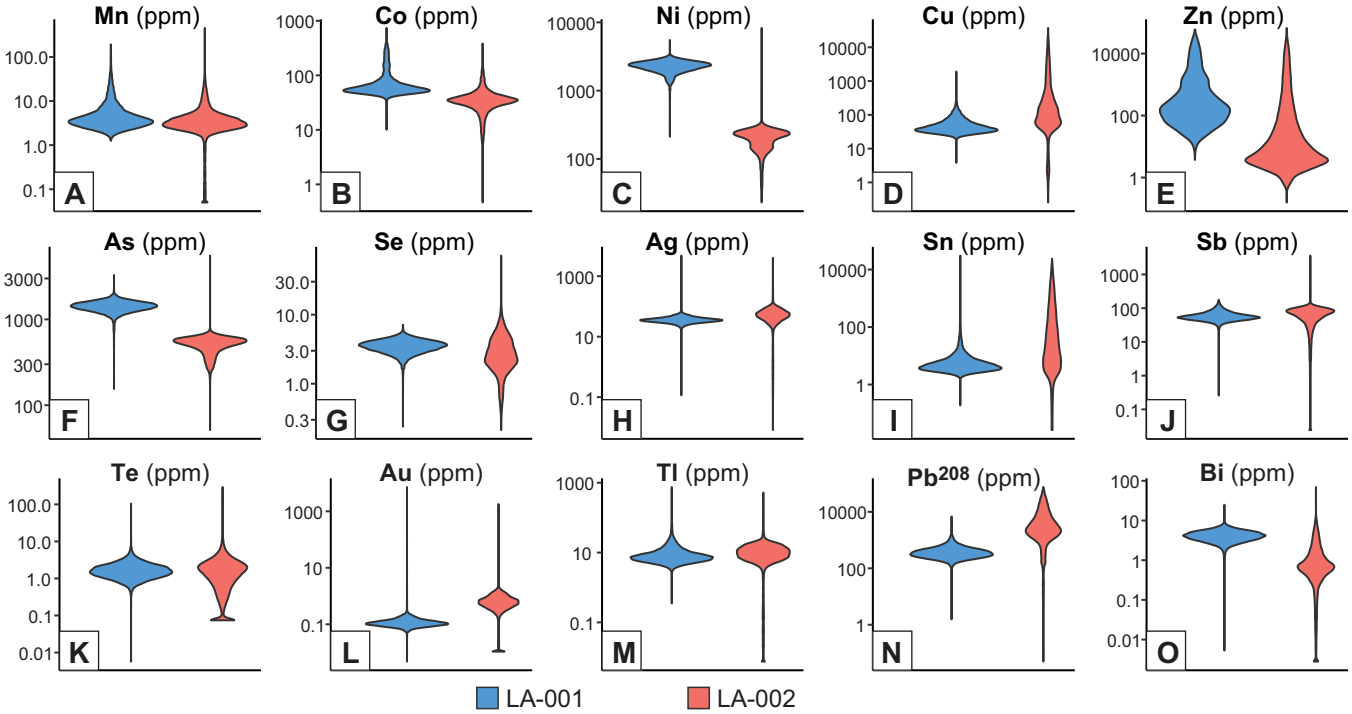

Figure 7. Violin plots of element abundances (ppm) in pyrite nodules LA-001 and LA-002: **a)** Mn, **b)** Co, **c)** Ni, **d)** Cu, **e)** Zn, **f)** As, **g)** Se, **h)** Ag, **i)** Sn, **j)** Sb, **k)** Te, **l)** Au, **m)** Tl, **n)** Pb, and **o)** Bi. The data are derived from the respective 13,494 and 29,662 analyses obtained by LA-ICP-MS. The thickness of each violin is proportional to the density of the values, and the length (including tails) represents the range of values:

accelerated into the mass spectrometer using a potential of 4.5 keV. The instrument was operated with a 150 µm diameter contrast aperture, and entrance and exit slits paired to give flat-topped peaks at a mass resolving power (MRP) of ≥2975 (10% peak height definition), which is sufficient to discriminate $^{33}SH^-$ (and $^{32}SH_2^-$) from $^{34}S^-$. A sample offset voltage of -60 eV and an energy window of 40 eV were also deployed. Overall reproducibility, based on replicate standard analyses, was typically better than ±0.4‰ (1σ). Complete details of the analytical methods, including the performance of in-house sulphide mineral stan-

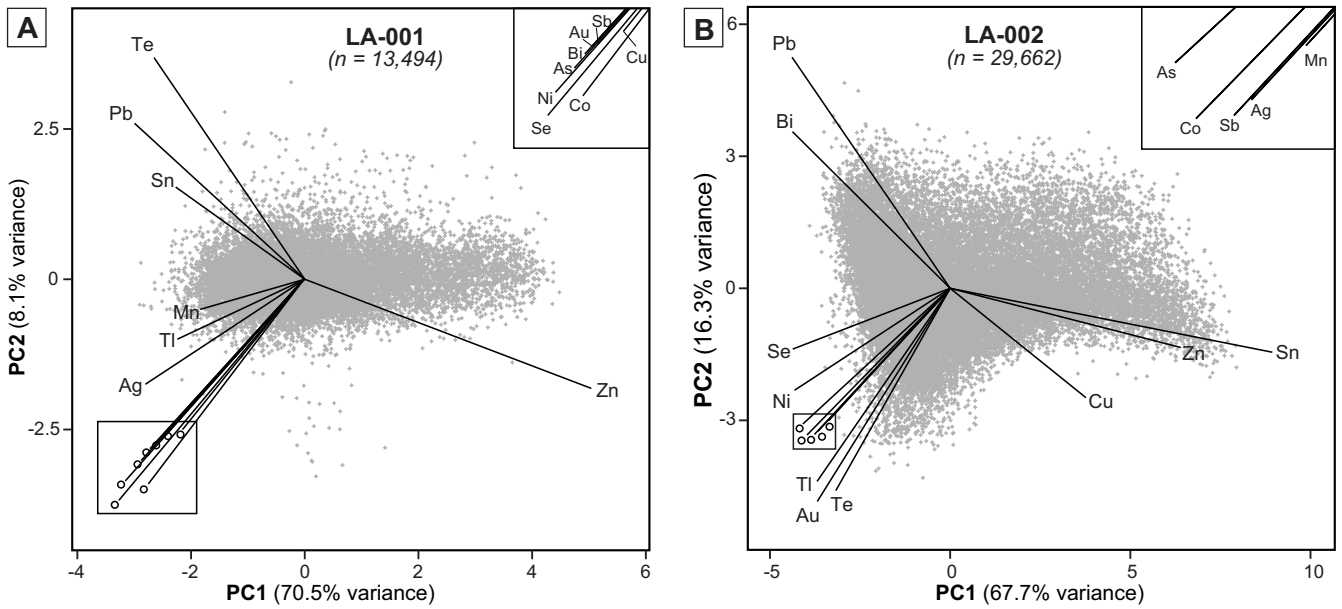

Figure 8. Bivariate plots of PC1 versus PC2 for **(a)** LA-001 and **(b)** LA-002 pyrite nodule data sets. In (a), PC1 and PC2 account for 70.5% and 8.1% of the variances, respectively. In (b), PC1 and PC2 account for 67.7% ad 16.3% of the variances, respectively.

Table 2. Secondary ion mass spectrometry in situ $\delta^{34}S$ stable isotopic data of pyrite nodules from the LaRonde Penna deposit.

Analysis	$\delta^{34}S$ VCDT (‰)	1s(SEM) (‰)	$^{34}S/^{32}S$ ratio	2SD ratio	SEM (%)	Poisson (%)	N cycles	Analyzed area
Nodule LA-001								
PML1 Py1	3.8	0.2	0.043919	0.000177	0.024	0.027	72	Zone 3: overgrowth
PML1 Py2	3.2	0.2	0.043895	0.000176	0.023	0.025	77	Zone 3: overgrowth
PML1 Py3	2.6	0.2	0.043866	0.000135	0.018	0.026	72	Zone 2c: Radial, bladded rim
PML1 Py4	1.9	0.2	0.043838	0.000147	0.019	0.025	76	Zone 2b: inclusion-rich concentric zone
PML1 Py5	1.8	0.2	0.043835	0.000158	0.021	0.026	76	Zone 2c: Radial, bladded rim
PML1 Py6	2.1	0.2	0.043846	0.000170	0.023	0.027	72	Zone 2b: inclusion-rich concentric zone
PML1 Py7	1.7	0.2	0.043828	0.000171	0.023	0.026	75	Zone 2b: inclusion-rich concentric zone
PML1 Py8	3.3	0.2	0.043900	0.000163	0.022	0.027	73	Zone 2b: inclusion-rich concentric zone
PML1 Py9	2.1	0.2	0.043845	0.000150	0.020	0.025	76	Zone 2b: inclusion-rich concentric zone
PML1 Py10	2.2	0.2	0.043849	0.000153	0.021	0.026	71	Zone 2a: Fine-grained inner rim
PML1 Py11	2.9	0.2	0.043882	0.000142	0.019	0.026	72	Zone 2a: Fine-grained inner rim
PML1 Py12	-0.6	0.2	0.043730	0.000167	0.022	0.026	76	Zone 1b: Recrystallized outer "clean" core
PML1 Py13	-0.8	0.2	0.043721	0.000180	0.023	0.026	77	Zone 1b: Recrystallized outer "clean" core
PML1 Py14	2.1	0.2	0.043846	0.000143	0.019	0.025	76	Zone 1a: Siliceous, inclusion-rich "gritty"core
PML1 Py15	1.8	0.2	0.043831	0.000134	0.017	0.025	77	Zone 1a: Siliceous, inclusion-rich "gritty"core
PML1 Py16	2.2	0.2	0.043851	0.000158	0.021	0.026	74	Zone 1a: Siliceous, inclusion-rich "gritty"core
PML1 Py17	1.9	0.2	0.043837	0.000144	0.019	0.026	76	Zone 1a: Siliceous, inclusion-rich "gritty"core
PML1 Py18	3.4	0.3	0.043902	0.000184	0.025	0.028	70	Zone 3: overgrowth
PML1 Py22	1.1	0.2	0.043802	0.000156	0.020	0.027	76	Zone 2b: inclusion-rich concentric zone
PML1 Py23	1.3	0.2	0.043812	0.000125	0.016	0.024	76	Zone 2a: Fine-grained inner rim
PML1 Py24	1.0	0.2	0.043797	0.000142	0.018	0.024	78	Zone 2a: Fine-grained inner rim
PML1 Py25	1.9	0.2	0.043836	0.000151	0.020	0.024	77	Zone 2a: Fine-grained inner rim
PML1 Py26	2.6	0.2	0.043866	0.000130	0.017	0.025	74	Zone 2a: Fine-grained inner rim
PML1 Py27	2.9	0.2	0.043879	0.000137	0.018	0.025	73	Zone 2c: Radial, bladded rim
PML1 Py28	2.2	0.2	0.043850	0.000157	0.021	0.024	75	Zone 2c: Radial, bladded rim
PML1 Py29	1.9	0.2	0.043837	0.000145	0.019	0.024	78	Zone 2b: inclusion-rich concentric zone
Nodule LA-002								
PML2 Py13	1.5	0.2	0.043819	0.000141	0.019	0.026	75	Zone 1: Siliceous, inclusion-rich "gritty" core
PML2 Py14	1.7	0.2	0.043827	0.000160	0.021	0.026	75	Zone 1: Siliceous, inclusion-rich "gritty" core
PML2 Py15	1.9	0.2	0.043838	0.000156	0.020	0.025	76	Zone 1: Siliceous, inclusion-rich "gritty" core
PML2 Py16	2.3	0.3	0.043853	0.000203	0.026	0.031	78	Zone 2c: Radial, bladded rim
PML2 Py17	0.0	0.2	0.043755	0.000175	0.023	0.028	77	Zone 2c: Radial, bladded rim
PML2 Py18	5.0	0.3	0.043974	0.000222	0.032	0.032	64	Zone 2c: Radial, bladded rim
PML2 Py19	3.2	0.3	0.043893	0.000218	0.030	0.031	68	Zone 3: overgrowth
PML2 Py20	1.5	0.3	0.043820	0.000210	0.028	0.029	73	Zone 2b: inclusion-rich concentric zone
PML2 Py21	0.1	0.2	0.043760	0.000185	0.024	0.029	76	Zone 2b: inclusion-rich concentric zone
PML2 Py22	1.6	0.2	0.043825	0.000169	0.022	0.029	75	Zone 2a: Fine-grained inner rim
PML2 Py23	2.2	0.2	0.043849	0.000176	0.024	0.030	72	Zone 2a: Fine-grained inner rim
PML2 Py1	1.7	0.2	0.043829	0.000163	0.022	0.027	73	Zone 3: overgrowth
PML2 Py2	3.5	0.3	0.043906	0.000200	0.027	0.028	73	Zone 2c: Radial, bladded rim
PML2 Py3	3.0	0.2	0.043884	0.000168	0.023	0.028	71	Zone 2c: Radial, bladded rim
PML2 Py4	3.9	0.3	0.043926	0.000188	0.025	0.025	71	Zone 2c: Radial, bladded rim
PML2 Py5	2.3	0.2	0.043855	0.000139	0.018	0.024	76	Zone 2c: Radial, bladded rim
PML2 Py6	2.2	0.2	0.043852	0.000115	0.015	0.024	72	Zone 2c: Radial, bladded rim
PML2 Py7	1.9	0.2	0.043836	0.000153	0.020	0.024	73	Zone 2b: inclusion-rich concentric zone
PML2 Py8	1.4	0.2	0.043813	0.000161	0.021	0.025	73	Zone 2b: inclusion-rich concentric zone
PML2 Py9	2.9	0.2	0.043881	0.000125	0.017	0.025	73	Zone 2a: Fine-grained inner rim
PML2 Py10	2.4	0.2	0.043861	0.000179	0.023	0.024	76	Zone 2a: Fine-grained inner rim
PML2 Py11	2.8	0.2	0.043877	0.000176	0.023	0.025	75	Zone 2a: Fine-grained inner rim
PML2 Py12	1.9	0.2	0.043836	0.000144	0.019	0.025	76	Zone 2a: Fine-grained inner rim

dards, their accepted $^{34}S/^{32}S$ ratios, and the calibration of instrument mass fractionation (IMF) factors, can be found in Brueckner et al. (2015).

Composition

Results for all the analyzed zones from both nodules are shown in Figure 9 and Table 2. From core to rim, including the overgrowth, the data average +2.1‰ (n = 50) and range between -0.8 and +5.0‰. In nodule LA-001, zone 1b (inclusion-free, equigranular pyrite that envelopes the gritty, inclusion-rich pyrite; Fig. 9b) shows the lowest $\delta^{34}S$ values (-0.8‰ and -0.6‰).

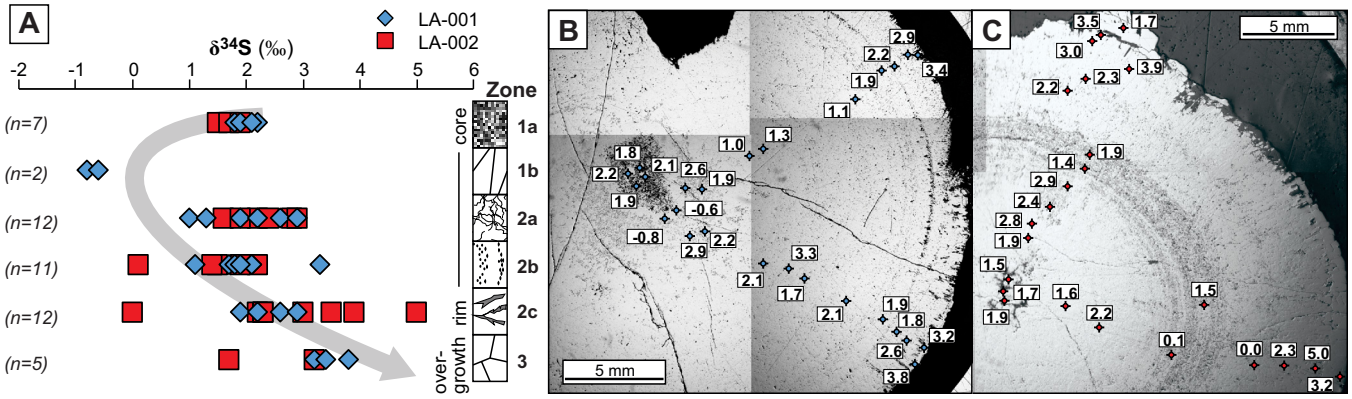

Figure 9. a) δ34S values of pyrite in each textural zone. **b and c**) Spot locations and δ34S values from SIMS analyses on pyrite nodules LA-001 and LA-002.

From the inner to the outer rim, despite some outliers, the isotopic values tend to become heavier (Fig. 9). The values for the overgrowth pyrite in nodule LA-001 are slightly higher than the rest of the nodule (+3.2 to +3.8‰), whereas the pyrite overgrowths from nodule LA-002 show values that overlap those of the outer rim (+1.7 and +3.2‰) (Table 2). Dubé et al. (2004) report $\delta^{34}S$ values (n = 6) from pyrite from the surrounding 20N Zn zone with an average of +2.2‰ and a range from +1.7 to +2.8‰. These are broadly consistent with the SIMS S-isotope data reported in the present study for nodules LA-001 and LA-002, which suggest a similar source of sulphur.

DISCUSSION

Pyrite nodules are common in many fine-grained sedimentary units (distal and proximal to mineralization) of the Abitibi greenstone belt and elsewhere in the Superior Province (Jonasson et al., 1999; Hannington et al., 2012; Pilote et al., 2019). Although many consider pyrite nodules diagenetic, certain aspects about their timing of formation and controls on their Au enrichment remain to be clarified, which constitute subjects of a larger study about nodules (Pilote et al., 2019, 2020). Here, the characteristics of nodule LA-001 and LA-002, which show a transition from a polycrystalline core to an envelope of radially oriented acicular grains of pyrite, are not unique to LaRonde, and appear to be similar to global examples from low-temperature-related diagenetic pyrite nodules from unmetamorphosed sequences (e.g. Rickard, 2012; Jeans et al., 2016).

Crystal growth is regulated by the degree of departure from equilibrium state (Sunagawa, 2005; Hu et al., 2019) and, for pyrite nodules in sedimentary rocks, the degree of supersaturation of the main reactant agents in hydrothermal or diagenetic fluids (i.e. Fe(II) and S(-II)) is the main driving factor. In sedimentary settings, concentrations of reduced Fe and S required to nucleate and form pyrite can be achieved in pore fluids without a hydrothermal contribution (Rickard, 2012). Pyrite growth will stop when the rate of supply of the reactant agents is less than the rate of crystal growth (i.e. equilibrium is reached). Some workers suggest that the transition from irregular-shaped, fine-grained crystals (core) to elongated, well defined crystal habits (rim) reflects a decrease in the degree of supersaturation (Murowchick and Barnes, 1987; Rickard, 2012; Hu et al., 2019), which also likely dictates the ability to concentrate trace elements (including Au). In pyrite nodules LA-001 and LA-002, Au is concentrated and controlled by the transition from fine-grained to bladed pyrite. The analytical approach used here does not allow us to recognize if Au occurs as a solid solution in pyrite lattices (e.g. Reich et al., 2005; Gregory et al., 2015) or as nanoparticles (Palenik et al., 2004; Fougerouse et al., 2016), but its core-restricted distribution suggests that the enrichment is related to the early formation of the nodules, possibly during a time of a high degree of supersaturation.

A similar core-to-rim decrease in Au abundance is common in pyrite nodules from the Timmins region (Pilote et al., 2019), and whereas most nodules from Timmins also show a decrease in trace elements, the LaRonde nodules exhibit some distinct patterns. Studies of Pilote et al. (2019, 2020) show that the contents of Ni and Tl (two relatively abundant trace elements that provide good discriminants for nodules (diagenetic) versus pyrite of epigenetic origins (e.g. porphyroblasts, granoblasts) within argillites) in the Timmins nodules decrease from core to rim, but with relatively less variability in Tl than Ni. This is expressed as a decrease in both Au and Ni/Tl on a bivariate plot (Fig. 10). In the LaRonde nodules, however, the opposite is observed (Fig. 10) and Ni/Tl increases at the expense of Au. Thallium bonds 'loosely' to pyrite crystal lattices (George et al., 2019), and Deditius and Reich (2016) suggested that its concentration in pyrite is controlled mainly by the abundances of trivalent Sb and As. The covariation

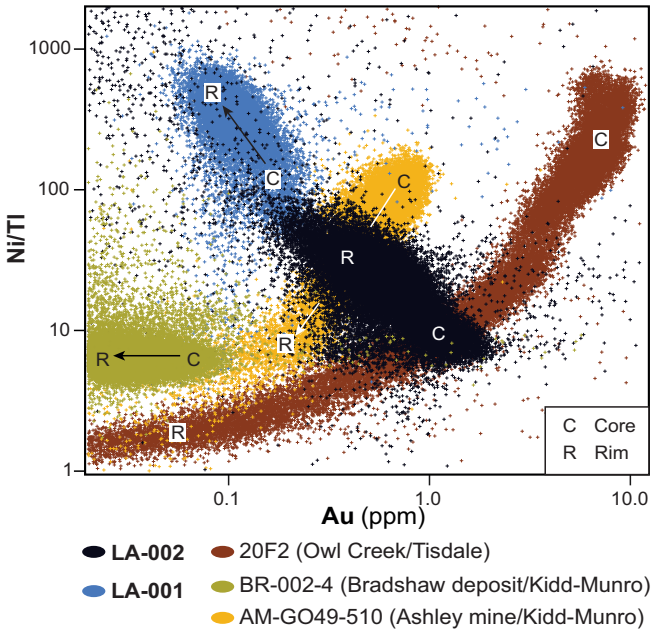

Figure 10. Gold (ppm) versus Ni/Tl from LA-ICP-MS element maps. Nodules LA-001 and LA-002 are compared to three representative nodules from the Timmins region (data from Pilote et al., unpublished): 1) nodule BR-002-4 from the Bradshaw deposit, 2) nodule AM-GO49-510 from the Ashley Mine, and 3) nodule 20F2 from the Owl Creek deposit.

observed for these three elements in the LaRonde pyrite nodules (Fig. 5h,l,p, 6h,l,p) concurs with this hypothesis. Moreover, Huston et al. (1995) suggest that the rate at which pyrite precipitates regulates the amount of Tl that it can accommodate. If correct, this would suggest that the cores precipitate at a faster rate than their surrounding rim. As for Ni, its enrichment in sediments is commonly suggested to be the result of hydrogenous adsorption onto metastable iron sulphides (e.g. mackinawite, although its presence in natural environments is debated; Rickard, 2012; Gregory et al., 2019) and/or of formation of organometallic complexes in reducing marine conditions (Tribovillard et al., 2006; Wilkin and Beak, 2017; Gadd et al., 2019). Diagenetic breakdown of the transporting agent would then release Ni (along with other trace elements) to be concentrated in the early formed pyrite (Tribovillard et al., 2006; Large et al., 2011). Given the relatively late Ni enrichment in the LaRonde nodules, this process is questionable, but more work is needed to substantiate this interpretation and test the mechanisms that led to Ni enrichment. The increase in Ni values in nodule LA-002 correlates with an increase in the abundance of stannite, sphalerite, and galena inclusions that is also reflected by an increase of Sn, Cu, Zn, Pb, and Bi. Similar minerals, in trace amounts, are present in the 20N Zn zone, although with evidence of recrystallization/replacement (Dubé et al., 2004). It would be reasonable to argue that a contribution from the ore-forming hydrothermal fluids during the growth of the nodule would explain the sudden appearance of these minerals in the nodules. However, this argument faces an important obstacle, and that is the type of hydrodynamic regime required to form large, concentrically zoned, nodular-shaped pyrite (Rickard, 2012). In order to maintain this texture, the supply of reactant agents (reduced Fe and S) has to be constant and the growth relatively rapid, with a gentle to nearly stagnant hydrodynamic regime (Rickard, 2012). These requirements can only be achieved in a closed or highly isolated system (Gregory et al., 2019) and a case for a direct hydrothermal contribution is difficult to support given the strong advective and open regime of a VMS system. Alternatively, instead of direct hydrothermal input, elements Sn, Cu, Zn, Pb, and Bi could have been enriched in the sediment (from nearby hydrothermal venting) at the time of deposition and partitioned into pyrite during diagenetic formation, before or after the formation of the 20 North lens.

The hourglass-shaped distribution of Cu, Zn, Sn, Pb and Bi observed in nodule LA-002 (Fig. 6f,g,k,q,r) from the sphalerite, stannite, and galena inclusions, which is parallel to the main elongation, is likely the product of deformation. Partial recrystallization of the rim in nodule LA-002 could have accommodated the liberation and/or reorganization of elements parallel to the plane of flattening.

We speculate that the strong variability in trace element abundances (e.g. Au, Ni, As; Fig. 7) in the nodules could be explained by differences in the host sediment composition, which are largely governed by its provenance (detrital versus hydrothermal). The possible compositional effects of the sediments (and source) on the pyrite compositions are currently being investigated in the Timmins region (Pilote et al., in prep). Lastly, an overall decrease in trace element abundance from the core to the rim, accompanied by an increase in $\delta^{34}S$ values, as in the LaRonde nodules, is also a common phenomenon. Gregory et al. (2019) report similar trends in nodules from Western Australia, the Urals, and Tasmania from sedimentary sequences of Neoarchean, Mesoproterozoic, and Cambrian ages, respectively. To explain the increase in $\delta^{34}S$ values observed in pyrite nodules LA-001 and LA-002, the authors suggest the progressive relative depletion of light S from bacterial sulphate reduction (BSR) activity in a closed or highly isolated system.

EXPLORATION IMPLICATIONS

Despite the limited number of samples, the presence of galena and stannite in close association with sphalerite inclusions in one of the pyrite nodules from an argillite lens within the 20N Zn orebody is interpreted as a signature of the hydrothermal activity that formed the enclosing mineralization. The preliminary results sug-

gest that a large portion of the enrichment in Sn, Zn, and Cu relates to a synsedimentary deposition process, prior to the nodule formation. Regardless, from an exploration perspective, the ore-like mineralogy and consequent chemical composition recorded by authigenic argillite-hosted pyrite nodules could potentially be used as a vector proxy for mineralization (contingent on a larger sample population from a wider distribution). While important questions remain, pyrite (and commonly pyrrhotite) nodules in argillitic sequences near VMS deposits are common in the Abitibi greenstone belt (e.g. pyrite nodules proximal to the main orebodies at Kidd Creek; Hannington et al., 1999a); however, detailed studies on their compositions in a well constrained metallogenic context are scarce. It should be noted that the presence of nodules alone should not be considered as a proxy for mineralization since they commonly form, as aforementioned, diagenetically and do not require hydrothermal fluids, which could be in fact an inhibiting factor if otherwise involved.

ONGOING AND FUTURE WORK

More robust comparisons are being made between nodules from LaRonde and the Timmins-Matheson gold corridor using multivariate statistical tools (i.e. PCA and linear discriminate analysis) to classify sedimentary pyrite generations as a function of their chemical assemblages ("clustering"). This approach will improve our understanding of the factors that control their genesis and auriferous nature. Gold enrichment in the core of nodules is very common but its genetic link with VMS systems remains poorly understood. Also, although the decrease in gold tenor from the core to the rim is likely related to the degree of supersaturation during pyrite growth, the cause of variability in gold content in the core from one nodule to another is still poorly understood.

ACKNOWLEDGMENTS

The authors wish to acknowledge Agnico Eagle Mines Ltd. and the LaRonde Penna mine personnel for having shared their knowledge of the LaRonde Penna deposit, for logistical and scientific support, and authorization to publish. A. de Coninck (INRS-ETE) helped with scanning electron microscope analyses. This contribution was reviewed by S. Paradis and D. Gregory.

REFERENCES

Brueckner, S.M., Piercey, S.J., Layne, G.D., Piercey, G., and Sylvester, P.J., 2015. Variations of sulphur isotope signatures in sulphides from the metamorphosed Ming Cu(-Au) volcanogenic massive sulphide deposit, Newfoundland Appalachians, Canada; Mineralium Deposita, v. 50, p. 619–640.

Davis, D.W., 2002. U-Pb geochronology of Archean metasedimentary rocks in the Pontiac and Abitibi Subprovinces, Quebec, constraints on timing, provenance and regional tectonics; Precambrian Research, v. 115, p. 97–117.

Deditius, A.P. and Reich, M., 2016. Constraints on the solid solubility of Hg, Tl, and Cd in arsenian pyrite; American Mineralogy, v. 101, p. 1451–1459.

Dubé, B., Mercier-Langevin, P., Hannington, M.D., Davis, D., and Lafrance, B., 2004. Le gisement de sulfures massifs aurifères volcanogènes LaRonde, Abitibi, Québec: altérations, minéralisations et implications pour l'exploration; Ministère des Ressources naturelles, de la Faune et des Parcs du Québec, MB 2004-03, 112 p.

Dubé, B., Gosselin, P., Mercier-Langevin, P., Hannington, M.D., and Galley, A., 2007a. Gold-rich volcanogenic massive sulphide deposits; *in* Mineral Deposits of Canada: A Synthesis of Major Deposit Types, District Metallogeny, the Evolution of Geological Provinces, and Exploration Methods, (ed.) W.D. Goodfellow; Geological Association of Canada, Mineral Deposits Division, Special Publication No. 5, p. 75–94.

Dubé, B., Mercier-Langevin, P., Hannington, M.D., Lafrance, B., Gosselin, G., and Gosselin, P., 2007b. The LaRonde Penna world-class Au-rich volcanogenic massive sulfide deposit, Abitibi, Québec: Mineralogy and geochemistry of alteration and implications for genesis and exploration; Economic Geology, v. 102, p. 633–666.

Dubé, B., Mercier-Langevin, P., Kjarsgaard, I., Hannington, M.D., Bécu, V., Côté, J., Moorhead, J., Legault, M., and Bédard, N., 2014. The Bousquet 2-Dumagami world-class Archean Au-rich volcanogenic massive sulfide deposit, Abitibi, Quebec: Metamorphosed submarine advanced argillic alteration footprint and genesis; Economic Geology, v. 109, p. 121–166.

Filzmoser, P., Hron, K., and Reimann, C., 2009. Principal component analysis for compositional data with outliers; Environmetrics, v. 20, p. 621–632.

Fougerouse, D., Reddy, S.M., Saxey, D.W., Rickard, W.D.A., van Riessen, A., and Micklethwaite, S., 2016. Nanoscale gold clusters in arsenopyrite controlled by growth rate not concentration: Evidence from atom microscopy; American Mineralogist, v.101, p. 1916–1919.

Gadd, M.G., Peter, J.M., Jackson, S.E., Yang, Z., and Petts, D., 2019. Platinum, Pd, Mo, Au and Re deportment in hyper-enriched black shale Ni-Zn-Mo-PGE mineralization, Peel River, Yukon, Canada; Ore Geology Reviews, v. 107, p. 600–614.

George, L.L., Biagioni, C., Orazio Lepore, G., Lacalamita, M., Agrosì, G., Carlo Capitani, G., Bonaccorsi, E. and d'Acapito, F., 2019. The speciation of thallium in (Tl,Sb,As)-rich pyrite; Ore Geology Reviews, v. 107, p. 364–380.

Gregory, D., Large, R.R., Halpin, J.A., Baturina, E.L., Lyons, T.W., Wu, S., Danyushevsky, L., Sack, P., Chappaz, A., Maslennikov, V.V., and Bull, S.W., 2015. Trace element content of sedimentary pyrite in black shales; Economic Geology, v. 110, p. 1389–1410.

Gregory, D., Mukherjee, I., Olson, S.L., Large, R.R., Danyushevsky, L.V., Stepanov, A.S., Avila, J.N., Cliff, J., Ireland, T.R., Raiswell, R., Olin, P.H., Maslennikov, V.V., and Lyons, T.W., 2019. The formation mechanisms of sedimentary pyrite nodules determined by trace element and sulfur isotope microanalysis; Geochimica et Cosmochimica Acta, v. 259, p. 53–68.

Guy, B.M., Beukes, N.J., and Gutzmer, J., 2010. Paleoenvironmental controls of pyrite from non-conglomeratic sedimentary rocks of the Mesoarchean Witwatersrand Supergroup, South Africa; South African Journal of Geology, v. 113, p. 195–228.

Guy, B.M., Ono, S., Gutzmer, J., Lin, Y., and Beukes, N.J., 2014. Sulfur sources of sedimentary "buckshot" pyrite in the Auriferous Conglomerates of the Mesoarchean Witwatersrand

and Ventersdorp Supergroups, Kaapvaal Craton, South Africa; Mineralium Deposita, v. 49, p. 751–775.

Halicz, L. and Günther, D., 2004. Quantitative analysis of silicates using LA-ICP-MS with liquid calibration; Journal of Analytical Atomic Spectrometry, v. 19, p. 1539–1545.

Hannington, M.D., Bleeker, W., and Kjarsgaard, I., 1999a. Sulfide mineralogy, geochemistry, and ore genesis of the Kidd Creek deposit: Part I. North, Central, and South Orebodies; *in* The Giant Kidd Creek Volcanogenic Massive Sulfide Deposit, western Abitibi Subprovince, Canada, (ed.) M.D. Hannington and C.T. Barrie; Society of Economic Geologists, Monograph 10, p. 163–224.

Hannington, M.D., Poulsen, K.H., Thompson, J.F.H., and Sillitoe, R.H., 1999b. Volcanogenic gold in the massive sulfide environment; Reviews in Economic Geology, v. 8, p. 325–356.

Hannington, M.D., de Ronde, C.E.J., and Petersen, S., 2005. Seafloor tectonics and submarine hydrothermal systems; *in* 100th Anniversary Volume (1905–2005), (ed.) J.W. Hedenquist, J.F.H. Thompson, R.J. Goldfarb, J.P. Richards; Society of Economic Geologists, p. 111–141.

Hannington, M.D., Coombs, A., van Hees, G., Duff, S., and Campos-Alvarez, N., 2012. Regional lithogeochemical study of the Kidd–Munro MEGATEM® survey areas, Timmins–Kirkland Lake, northern Ontario: Discover Abitibi Initiative; Ontario Geological Survey, Miscellaneous Release Data 291, 209 p.

Hu, S., Barnes, S.J., Glenn, A.M., Pagès, A., Parr, J., MacRae, C., and Binns, R., 2019. Growth history of sphalerite in a modern sea floor hydrothermal chimney revealed by electron backscattered diffraction; Economic Geology, v. 114, p. 165–176.

Huston, D.L., Sie, S.H., Suter, G.F., Cooke, D.R., and Both, R.A., 1995. Trace elements in sulfide minerals from eastern Australian volcanic-hosted massive sulfide deposits; Part I, Proton microprobe analyses of pyrite, chalcopyrite, and sphalerite, and Part II, Selenium levels in pyrite; comparison with delta ^{34}S values and implications for the source of sulfur in volcanogenic hydrothermal systems; Economic Geology, v. 90, p. 1167–1196.

Jackson, S.E., 2008. LAMTRACE data reduction software for LA-ICP-MS; *in* Laser ablation-ICP-mass spectrometry in the Earth sciences: Current practices and outstanding issues, (ed.) P. Sylvester; Mineralogical Association of Canada, Short Course Series, v. 40, p. 305–307.

Jeans, C.V., Turchyn, A.V., and Hu, X., 2016. Sulfur isotope patterns of iron sulfide and barite nodules in the Upper Cretaceous Chalk of England and their regional significance in the origin of coloured chalks; Acta Geologica Polonica, v. 66, p. 227–256.

Jonasson, I.R., Kingston, D.M., Watkinson, D.H., and Elliot, S.R., 1999. Role of pyrite in the formation and localisation of gold mineralization at the Owl Creek mine, Timmins, Ontario; *in* The Giant Kidd Creek Volcanogenic Massive Sulfide Deposit, western Abitibi Subprovince, Canada, (ed.) M.D. Hannington and C.T. Barrie; Society of Economic Geologists, Monograph 10, p. 627–660.

Lafrance, B., Moorhead, J., and Davis, D.W., 2003. Cadre géologique du camp minier de Doyon-Bousquet-LaRonde: Ministère des Ressources Naturelles, de la Faune et des Parcs du Québec, ET 2002-07, 45 p.

Large, R.R., Maslennikov, V.V., Robert, F., Danyushevsky, L.V., and Chang, Z., 2007. Multistage sedimentary and metamorphic origin of pyrite and gold in the Giant Sukhoi log deposit, Lena Gold Province, Russia; Economic Geology, v. 102, p. 1233–1267.

Large R.R., Bull S.W., and Maslennikov V.V., 2011. A carbonaceous sedimentary source-rock model for Carlin-type and orogenic gold deposits: Economic Geology, v. 106, p. 331–358.

Large, R.R., Halpin, J.A., Danyushevsky, L.V, Maslennikov, V.V., Bull, S.W., Long, J.A., Gregory, D., Lounejeva, E., Lyons, T.W., Sack, P., McGoldrick, P., and Calver, C.R., 2014. Trace element content of sedimentary pyrite as a new proxy for deep-time ocean-atmosphere evolution; Earth and Planetary Science Letters, v. 389, p. 209–220.

McNicoll, V., Goutier, J., Dubé, B., Mercier-Langevin, P., Ross, P.S., Dion, C., Monecke, T., Legault, M., Percival, J., and Gibson, H., 2014. U-Pb geochronology of the Blake River Group, Abitibi greenstone belt, Quebec, and implications for base metal exploration; Economic Geology, v. 109, p. 27–59.

Mercier-Langevin, P., Dubé, B., Lafrance, B., Hannington, M., Galley, A., Moorhead, J., and Gosselin, P., 2007a. Metallogeny of the Doyon-Bousquet-LaRonde mining camp, Abitibi greenstone belt, Quebec; *in* Mineral Deposits of Canada: A Synthesis of Major Deposit Types, District Metallogeny, the Evolution of Geological Provinces, and Exploration Methods, (ed.) W.D. Goodfellow; Geological Association of Canada, Mineral Deposits Division, Special Publication No. 5, p. 673–701.

Mercier-Langevin, P., Dubé, B., Hannington, M.D., Davis, D.W., Lafrance, B., and Gosselin, G., 2007b. The LaRonde Penna Au-rich volcanogenic massive sulfide deposit, Abitibi greenstone belt, Quebec: Part I. Geology and geochronology; Economic Geology, v. 102, p. 585–609.

Mercier-Langevin, P., Dubé, B., Hannington, M.D., Richer-Laflèche, M., and Gosselin, G., 2007c. The LaRonde Penna Au-rich volcanogenic massive sulfide deposit, Abitibi greenstone belt, Quebec: Part II. Lithogeochemistry and paleotectonic setting; Economic Geology, v. 102, p. 611–631.

Mercier-Langevin, P., Dubé, B., Blanchet, F., Pitre, D., and Laberge, A., 2017. The LaRonde Penna Au-rich volcanogenic massive sulfide deposit; *in* Reviews in Economic Geology; Society of Economic Geologists, v. 19, p. 225–245.

Monecke, T., Gibson, H., Dubé, B., Laurin, J., Hannington, M.D., and Martin, L., 2008. Geology and volcanic setting of the Horne deposit, Rouyn-Noranda, Quebec: Initial results of a new research project; Geological Survey of Canada, Current Research 2008-9, 16 p.

Monecke, T., Gibson, H., Huthmann, F., Dubé, B., Hannington, M.D., McNicoll, V., and Mercier-Langevin, P., 2009. Giant volcanogenic massive sulphide deposits of the Blake River Group: Current knowledge and implications for exploration Part II – Horne; Congrès Abitibi 2009 – Abitibi Cuivre, Rouyn-Noranda, September 28th, 2009, Excursion Guidebook, GM 64196, p. 51–60.

Monecke, T., Mercier-Langevin, P., Dubé, B., Frieman, B., and Goutier, J., 2017. Geology of the Abitibi greenstone belt; Reviews in Economic Geology, v. 19, p. 7–49.

Murowchick, J.B. and Barnes, H.L., 1987. Effects of temperature and degree of supersaturation on pyrite morphology; American Mineralogist, v. 72, p. 1241–1250.

Palenik, C.S., Utsunomiya, S., Reich, M., Kesler, S.E., Wang, L., and Ewing, R.C., 2004. "Invisible" Au revealed: Direct imaging of Au nanoparticles in a Carlin-type deposit; American Mineralogist, v. 89, p. 1359–1366.

Pilote, J.-L., Jackson, S.E., Mercier-Langevin, P., Dubé, B., and Rhys, D., 2019. Characteristics of diagenetic and epigenetic sulphides in deformed and metamorphosed Archean carbonaceous metasedimentary rocks of the Timmins-Matheson corridor: establishing a framework for fingerprinting ore-forming processes in shear zone-hosted orogenic gold systems; *in* Targeted Geoscience Initiative: 2018 report of activities, (ed.) N. Rogers; Geological Survey of Canada, Open File 8549, p. 33–41.

Pilote, J.-L., Jackson, S.E., Mercier-Langevin, P., Dubé, B., Lawley, C.J.M., Petts, D.C., Yang, Z., van Hees, E., and Rhys, D., 2020. Fingerprinting ore processes in orogenic auriferous systems: Insights into metallogenic and exploration implica-

tions from argillite-hosted iron sulphide nodules from the Timmins-Matheson gold corridor; *in* Targeted Geoscience Initiative 5: Contributions to the Understanding of Canadian Gold Systems, (ed.) P. Mercier-Langevin, C.J.M. Lawley, and S. Castonguay; Geological Survey of Canada, Open File 8712, p. 165–178. doi:10.4095/323675

R Core Team, 2019. R: A language and environment for statistical computing; R Foundation for Statistical Computing, Vienna, Austria. <https://www.R-project.org/>

Reich, M., Kesler, S.E., Utsunomiya, S., Palenik, C.S., Chryssoulis, S.L., and Ewing, R.C., 2005. Solubility of gold in arsenian pyrite; Geochimica et Cosmochimica Acta, v. 69, p. 2781–2796.

Rickard, D.T., 2012. Sulfidic sediments and sedimentary rocks: Developments in sedimentology; Amsterdam, Elsevier, 816 p.

Sillitoe, R.H., Hannington, M.D., and Thompson, J.F.H., 1996. High sulfidation deposits in the volcanogenic massive sulfide environment; Economic Geology, v. 91, p. 204–212.

Sunagawa, I., 2005. Crystals: growth, morphology, and perfection; Cambridge, Cambridge University Press, 295 p.

Tribovillard, N., Algeo, T.J., Lyons, T., and Riboulleau, A., 2006. Trace metals as paleoredox and paleoproductivity proxies: An update; Chemical Geology, v. 232, p. 12–32.

Wilkin, R.T. and Beak, D.G., 2017. Uptake of nickel by synthetic mackinawite; Chemical Geology, v. 462, p. 15–29.